Role of excited atoms in decaying low-pressure argon plasma

Sergey Gorchakov,* Detlef Loffhagen, and Dirk Uhrlandt
INP Greifswald, Friedrich-Ludwig-Jahn-Straße 19, Greifswald 17489, Germany
(Received 12 September 2006; published 5 December 2006)

The influence of the kinetics of excited atoms on the characteristics of an inductively coupled plasma in argon during the early afterglow is studied. A self-consistent model including the nonlocal approach for the kinetic treatment of the electrons is applied. Parameters of both the steady state of the rf discharge and the decay phase are presented. Results for the steady-state densities of excited atoms as well as temporal evolutions of the wall potential and mean energy of electrons are discussed in comparison with experimental data available from the literature. The ionization kinetics of the electrons, the electron power balance, and the main kinetic pathways for excited argon atoms are analyzed in the pressure range between 0.5 and 133 Pa. In particular, a significant influence of the excited atoms on the plasma behavior in steady state and during the afterglow is found.

DOI: 10.1103/PhysRevE.74.066401 PACS number(s): 52.80.Hc, 52.25.Dg, 52.50.Qt

I. INTRODUCTION

Pulsed low-pressure discharges have been of permanent interest for many years. This is mainly caused by their use, e.g., as light sources and for plasma processing. Specific features of these discharges, in particular their high values of the electron density and mean electron energy, make possible the initiation and control of a manifold of radiation, chemical, and surface processes activated by the discharge plasma. When pulsed operation is used, the decay phase of the discharge can have a large impact on the time-averaged discharge characteristics and specific plasma properties. A detailed treatment of the time-dependent plasma parameters and of the complex particle interaction and redistribution processes is required not only in the active, but also in the afterglow phase of the discharge. These interaction processes can well be analyzed by means of numerical modeling.

At sufficiently high pressure, starting at few tens of pascals, the collisional interaction between the electrons and excited heavy particles considerably influences the plasma properties. Because of the low thresholds for exciting and ionizing collisions, these states participate both in the power dissipation processes and in the charge carrier generation of the plasma. In particular, the latter is controlled by stepwise and chemoionization processes, while the excitation, ionization, and superelastic collisions yield significant contributions to the power balance. However, when the pressure is decreased to a few pascals, other processes, like direct ionization and ambipolar diffusion, become predominant. Therefore, most of the models used so far to investigate low-presure plasmas often neglect the kinetics of excited species [1–6] or include only the most important processes and simplified kinetic schemes [7–12].

A number of recent experimental studies of argon discharges [13–16] have clarified that the densities of excited atoms could be sufficiently high to influence the characteristics of the discharge plasma even when the total gas pressure is in the order of a few pascals, i.e., a few tens of millitorrs. An experimental study of different regimes of a plasma of an inductively coupled discharge in argon [17] showed the important role of the electron impact excitation of excited states, in particular stepwise metastable excitation, during the off phase of the discharge. The effect is especially pronounced at pressures around 30 Pa. In the pulsed regime, the production of the higher excited states continues during the field-free phase, especially at pressures between 10 and 20 Pa as a result of stepwise excitation from lower excited states.

The effect of chemoionization processes on the electron energy probability function in the afterglow was clearly demonstrated in Ref. [18] where the results of experimental investigations of decaying helium and argon plasmas in a rf discharge were reported.

The impact of excited atoms in the active discharge phase starts at somewhat higher pressures. It was proven by quenching experiments in argon-nitrogen mixtures [7] that at pressures higher than 100 Pa the metastable argon atoms are responsible for an increase of the charge carrier density due to the stepwise ionization processes.

Fluid simulations of inductively coupled discharges in pure argon [19–21] predicted an important role of the metastable atoms. The inclusion of these excited atoms into the model [19] resulted in an increase of the discharge current mainly due to stepwise ionization processes and a decrease of the power dissipation and the sheath thickness in argon at 133 Pa. The recent theoretical investigations [20,21] based on simplified argon kinetics showed that even at the pressure of about 20 Pa the stepwise ionization contributes with more than 20% to the total ionization rate. These processes are responsible for the strong hysteresis of the plasma density in the active discharge, namely, a higher plasma density during the decreasing power phase in comparison with that during the increasing plasma phase [21]. Chemoionization processes are found of minor importance during the active phase of the discharge [20,21].

However, the situation changes in the absence of the external electric field. A theoretical study of the late afterglow in helium and argon plasmas [8] showed that superelastic collisions and chemoionization are very important processes

*Electronic address: gorchakov@inp-greifswald.de

for the particle and power budgets in decaying plasmas. Nevertheless, the role of stepwise ionization during this phase remains unclear, because corresponding processes were not included in that model.

The aim of the present paper is to analyze the influence of the excited states on the characteristics of both the active and decaying phases of a pulsed rf discharge. The range of the discharge parameters covers typical conditions from a plasma reactor to a discharge lamp. As an example, an inductively coupled argon discharge in a cylindrical vessel of few cm height is considered.

In a previous work [22] a model of the low-pressure argon afterglow plasma has been reported. The main features of this model are the description of electron kinetics by solving the space- and time-dependent Boltzmann equation using the nonlocal approach as well as the inclusion of collisional interaction between electrons and the gas, diffusive cooling, electron-electron collisions, and chemoionization processes. The model is applicable to describe both the active and the decay phases of the discharge. That way, the model avoids such approximations, like, e.g., the assumption of a Maxwellian distribution function for electrons, and takes into account all processes relevant for the pressure range of interest.

In the present paper an extension of this model [22], in particular by the inclusion of balance equations of the excited argon atoms, is applied. Details of the generalized model are given in Sec. II. The results of model calculations for excited atom densities and the ionization and power budget of the plasma are discussed in Sec. III and are evaluated by comparison with experimental data available from the literature.

II. BASIC FEATURES OF THE MODEL

The study has been performed for a diffusive plasma confined between relatively large dielectric or floating metal disks with a diameter D in a distance d. The discharge arrangement is discussed in detail in Ref. [22]. The plasma is produced by an azimuthal rf field at a field frequency of 13.56 MHz. In the framework of the theoretical treatment the discharge is assumed to be axially symmetric and spatially homogeneous in radial and azimuthal direction. Thus, the spatial dependence is reduced to the treatment of the plasma confinement by the time-dependent space-charge potential $V(z,t)$ in axial direction. A self-consistent model [22], which includes the time- and space-dependent electron kinetic equation, the system of fluid equations for various heavy particles and equations determining the axial space-charge potential has been adopted and generalized for the current investigations.

The kinetic description of the electrons requires the solution of the time- and space-dependent Boltzmann equation including the relevant collision integrals for elastic, exciting, deexciting, and ionizing electron-atom collisions as well as the electron-electron interaction and chemoionization. The kinetic equation of the electrons is simplified with respect to the treatment in velocity space by applying the two-term approximation of the expansion of the electron velocity distribution (EVD) function in spherical harmonics. The space-charge confinement and resulting spatial inhomogeneity in the kinetic equation is described by applying the nonlocal approach [5,23] in the axial direction (z), i.e., by the introduction of a total energy ε as sum of the electron kinetic energy u and the potential energy $w(z,t)=-e_0V(z,t)$ in the axial space-charge field and by averaging of the resulting equation over the axial coordinate [22]. Applying these assumptions, a partial integro-differential equation for the isotropic component $f_0(\varepsilon,t)$ of the EVD function finally results. The wall losses of the electrons are treated by a loss term in this kinetic equation, which vanishes for total energies lower than the potential energy corresponding to the space-charge potential at the wall. The corresponding electron particle and power flux toward the wall result from appropriate energy space averaging of this term of the kinetic equation.

The temporal behavior of the space-charge potential is determined by a simplified description considering an appropriate diffusion length of the ion flux to the wall and assuming a cosine form for the axial density profile of the argon ions. Following measurements under comparable conditions, an appropriate polynomial function for the axial profile of the space-charge potential has been adopted [22].

In order to analyze the impact of the argon kinetics on the discharge properties, a detailed reaction kinetic model has been developed and included into the self-consistent model. Within the argon energy levels 16 states are distinguished: the ground state $\mathrm{Ar}(1p_0)$ (here and further the Paschen notation is used) with a time- and space-independent density N_0, the 14 individual excited states $\mathrm{Ar}(1s_5)$ to $\mathrm{Ar}(1s_2)$ and $\mathrm{Ar}(2p_{10})$ to $\mathrm{Ar}(2p_1)$ with the densities $N_1(z,t)$ to $N_{14}(z,t)$, and the argon ion Ar^+ in the ground state.

Details of the basic equations of the excited atoms, of the atomic data used and of the solution method are given in the following subsections.

A. Balance equations of excited species

The spatiotemporal evolution of the densities of excited argon atoms $N_l(z,t)$ is described by corresponding time- and space-dependent balance equations. Taking into account the specified discharge geometry these equations get the form

$$\frac{\partial N_l}{\partial t} - D_l^m \frac{\partial^2 N_l}{\partial z^2} + N_l(\nu_l^{\mathrm{el}} + \nu_l^h) = P_l^{\mathrm{el}} + \sum_{k=5}^{14} \frac{N_k}{\tau_{k,l}} \quad (l = 1,3), \tag{1a}$$

$$\frac{\partial N_l}{\partial t} + N_l(\nu_l^{\mathrm{el}} + \nu_l^h) + \sum_{k=0}^{l-1} \frac{N_l}{\tau_{l,k}} = P_l^{\mathrm{el}} + P_l^h + \sum_{k=l+1}^{14} \frac{N_k}{\tau_{k,l}} \quad (l = 2,4,\ldots,14), \tag{1b}$$

where Eq. (1a) describes the behavior of the metastable atoms $\mathrm{Ar}(1s_5)$ and $\mathrm{Ar}(1s_3)$ and Eq. (1b) that of all other excited atoms. This system is complemented by the representations

$$\nu_l^{\mathrm{el}}(z,t) = n_e(z,t)\left(\sum_{k=0,k\neq l}^{14} z_{l,k}^{\mathrm{in}}(z,t) + z_l^{\mathrm{io}}(z,t)\right), \quad l = 1, \ldots 14, \tag{2a}$$

$$\nu_l^{h}(z,t) = 2\sum_{k=1}^{4} N_k(z,t) z_{l,k}^{\mathrm{ch}}, \quad l = 1, \ldots, 4, \tag{2b}$$

$$\nu_l^{h}(z,t) = N_0 \sum_{k=5,k<l}^{14} z_{l,k}^{\mathrm{Ar}}, \quad l = 5, \ldots, 14, \tag{2c}$$

$$P_l^{\mathrm{el}}(z,t) = n_e(z,t) \sum_{k=0,k\neq l}^{14} N_k(z,t) z_{k,l}^{\mathrm{in}}, \quad l = 1, \ldots, 14, \tag{2d}$$

$$P_l^{h}(z,t) = N_0 \sum_{k=5,k>l}^{14} N_k(z,t) z_{k,l}^{\mathrm{Ar}}, \quad l = 1, \ldots, 14, \tag{2e}$$

of the individual particle loss frequencies ν_l^{el} and ν_l^h and gain rates P_l^{el} and P_l^h. Here, $z_{l,k}^{\mathrm{in}}$ are the rate coefficients for exciting and deexciting electron collisions, z_l^{io} those of the electron impact ionization, and n_e is the time- and space-dependent electron density. These quantities are determined by appropriately averaging the isotropic distribution $f_0(\varepsilon,t)$ over the total energy according to

$$n_e(z,t) = \int_{\varepsilon=w(z,t)}^{\infty} \sqrt{u} f_0(\varepsilon,t) d\varepsilon, \tag{3}$$

$$z_\alpha^\beta(z,t) = \frac{1}{n_e(z,t)} \sqrt{\frac{2}{m_e}} \int_{\varepsilon=w(z,t)}^{\infty} u Q_\alpha^\beta(u) f_0(\varepsilon,t) d\varepsilon,$$
$$(\alpha;\beta) = (l,k;\mathrm{in}), \quad (l;\mathrm{io}), \tag{4}$$

where $Q_{l,k}^{\mathrm{in}}$ and Q_l^{io} are the total cross sections for the conservative inelastic (in) and ionizing (io) electron collision processes.

The coefficients D_l^m for the diffusion of the metastable argon atoms in argon have been taken from Ref. [24]. The consideration of the rate coefficients $z_{l,k}^{\mathrm{Ar}}$ and $z_{l,k}^{\mathrm{ch}}$ for quenching and chemoionization processes is detailed below.

The system of equations (1a) and (1b) has been solved using appropriate boundary conditions. In particular, the losses due to deexcitation at the wall surface are considered for the metastable atoms. Following the ideas of Ref. [25] the outflow of the metastable atoms toward the wall at z_e with the particle flux density $j_w(t) = \gamma N_k(z_e,t)$ has been fixed as boundary condition. Following the measurements of Ref. [16] a value of $\gamma = 7.5 \times 10^3$ cm/s was estimated.

B. Collisions with electrons

The set of electron-atom collisions has been selected from the literature. The data for excitation processes among the argon states have been compiled from the theoretical data set of Bartschat *et al.* [26–28], which was obtained by calculations using the Breit-Pauli *R*-matrix method. This cross section set coincides well with the measured total excitation cross section of Schaper and Scheibner [29] and recent experimental data for individual excitation of excited argon atoms of Boffard *et al.* [30]. The cross sections for deexcitation have been obtained according to the principle of detailed balancing. The cross section of direct ionization of argon atoms has been taken from Ref. [31]. Those for stepwise ionization have been calculated according to Deutsch-Märk formalism [32], which show good agreement with experimental data of Ref. [33]. The momentum transfer cross section for elastic electron-argon collisions was taken from Ref. [34].

TABLE I. Rate coefficients $z_{l,k}^{\mathrm{ch}}$ and the center $u_c^{l,k}$ and width $u_w^{l,k}$ of inscattering profile for chemoionization processes.

Reactants	$z_{l,k}^{\mathrm{ch}}$ ($\mathrm{cm}^3\,\mathrm{s}^{-1}$)	$u_c^{l,k}$ (eV)	$u_w^{l,k}$ (eV)
$\mathrm{Ar}(1s_5)+\mathrm{Ar}(1s_5)$	1.3×10^{-9}	7.32	1.5
$\mathrm{Ar}(1s_5)+\mathrm{Ar}(1s_4)$	4.5×10^{-10}	7.4	1.5
$\mathrm{Ar}(1s_5)+\mathrm{Ar}(1s_3)$	1.3×10^{-9}	7.5	1.5
$\mathrm{Ar}(1s_5)+\mathrm{Ar}(1s_2)$	4.5×10^{-10}	7.6	1.5
$\mathrm{Ar}(1s_4)+\mathrm{Ar}(1s_4)$	4.5×10^{-10}	7.48	1.5

C. Radiation processes

Radiative transitions between different argon levels have been included in the model. Because of the long lifetime of metastable levels the radiation from these levels was neglected. Even at a low pressure, the plasma cannot be assumed to be optically thin for the transitions from $\mathrm{Ar}(1s_4)$ and $\mathrm{Ar}(1s_2)$ levels into the ground state. In order to describe these processes, the effective lifetime approximation according to the Holstein theory of radiation trapping for a cylindrical plasma has been chosen for simplicity. The effective lifetimes $\tau_{2,0}$ and $\tau_{4,0}$ have been determined using the natural lifetimes of 8.4 and 1.96 ns, respectively [35]. For all other optically allowed transitions natural lifetimes of Refs. [35,36] have been used.

D. Heavy particle collision data

In the pressure range considered chemoionization is one of the most important processes of electron production. Furthermore, the chemoionization process is a source of electrons with relatively high energy and, therefore, it acts against the diffusive cooling of the electron gas. The contribution of this electron gain process to the electron particle and energy balance is proportional to the densities of the two colliding particles. Here, the ionizing collisions between the four lowest excited argon levels were taken into account. The rate coefficients $z_{l,k}^{\mathrm{ch}}$ $(l,k=1,\ldots,4)$ were estimated according to Ref. [37]. Table I gives the values of the rate coefficients as well as the characteristics of the inscattering profile (center and width of Gaussian function) used in the model.

Concerning the quenching kinetics of all excited states, the rate coefficients $z_{l,k}^{\mathrm{Ar}}$ for transitions from level l to level k for these processes were taken from Refs. [38–40].

E. Solution approach

The basics of the solution approach have already been presented in Ref. [22]. The main difference in the present method is an additional iteration over the densities of excited atoms by solving their balance equations. The initial parameters for the afterglow studies were calculated for given electron density. For each electron density value the rf field strength, the densities of excited atoms and the wall potential were varied until the steady-state values of all these quantities were established.

The afterglow starts at $t=0$ with switching off the rf field exponentially within 500 ns. For each time step the following iterative solution procedure was used for known rf field amplitude. First, a value of the space-charge potential at the new time is estimated. Next, the time-dependent kinetic equation of the electrons is solved for given densities of excited atoms. Using the resulting energy distribution function of the electrons, updated transport and rate coefficients and particle wall losses of the electrons are determined. These rate coefficients are used for the determination of the excited atom densities at the new time by solving Eqs. (1a) and (1b). These densities are employed then to solve again the kinetic equation. The cycle of alternating solution of the electron kinetic equation and the balance equations of excited atoms is continued until convergence with respect to the excited atom densities and the energy distribution is reached. Now, a new value of the wall potential is suggested, leading to a better compensation of the electron and ion fluxes at the wall and the iterative solution of the kinetic equation and balance equations is repeated again. The solution for the time step is finished when sufficient compensation of the electron and ion fluxes at the wall is also reached and a new time step can begin.

III. RESULTS AND DISCUSSION

Model calculations have been performed for argon discharges at pressures between 0.5 and 133 Pa and plasma powers in the range from 2 to 300 W. The temporal evolution of the decaying plasma ranging from the active discharge up to 100 μs after switching off the rf field has been analyzed. For given pressure the initial rf field amplitude was chosen so that the same spatially averaged electron energy density, i.e., fixed energy stored in the discharge, results. In order to compare the results of the modeling with the experimental data, two different reactor geometries have been considered: discharge geometry A with diameter $D=11.4$ cm and electrode gap $d=3.9$ cm, and discharge geometry B with $D=28$ cm and $d=10$ cm. Experimental results for the geometry A were taken from Ref. [16]. They include measurements of line-integrated densities of excited argon atoms. Results of probe measurements of the wall potential and mean electron energy in the discharge center from Ref. [3] were used for a comparison with modeling result for the discharge geometry B.

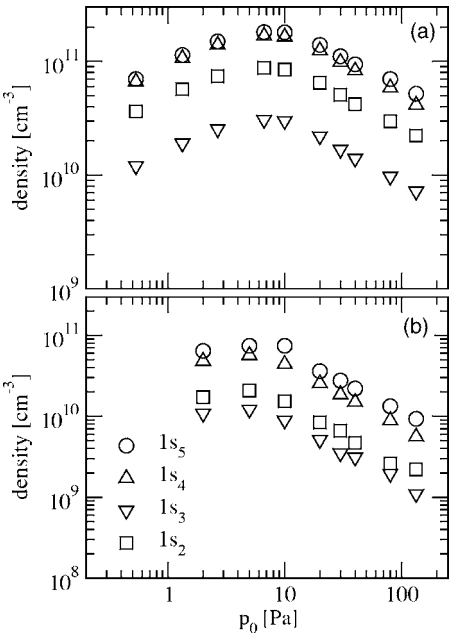

FIG. 1. Steady-state densities of excited argon atoms in the discharge center in dependence on the gas pressure for (a) discharge geometry A and (b) geometry B.

A. Densities of the excited argon atoms

In this section results of absolute and line-integrated densities of excited argon atoms are represented. Figure 1 shows the steady-state densities of the argon atoms $\mathrm{Ar}(1s_5)$ to $\mathrm{Ar}(1s_2)$ in the discharge center at $z=0$ for varying pressures p_0 and a constant energy density of the electrons of 30 μJ/cm^2. The model predicts a qualitatively similar pressure dependence for the different excited states and quite high densities even for the lowest pressure considered. Maximum values of all densities were obtained at a pressure of about 6 Pa for both geometries. The reason for the density increase at growing pressure below this value is the dominance of the processes of ground state excitation with increasing collision frequencies. Above 6 Pa the frequencies of electron impact excitation of excited states (stepwise excitation) grow substantially. Furthermore, at higher pressures the power losses due to elastic collisions become more and more important, and less power is dissipated in excitation processes. As a consequence, the densities of excited atoms decrease.

The inverse population of the $\mathrm{Ar}(1s_3)$ and $\mathrm{Ar}(1s_2)$ states with respect to their excitation energy occurs because of the higher excitation rates of $\mathrm{Ar}(1s_2)$ from the ground state and was confirmed by experiments for geometry A [16].

To illustrate the spatial dependence of the excited atoms, their temporal decay, and a comparison with experimental data, only results for geometry A are represented in the following. Similar results were found for geometry B.

Axial profiles of the densities of excited argon atoms for geometry A are displayed in Fig. 2 for a pressure of 1.33 Pa. The space-charge confinement leads to a pronounced axial decrease in the electronic excitation rates. Therefore, all den-

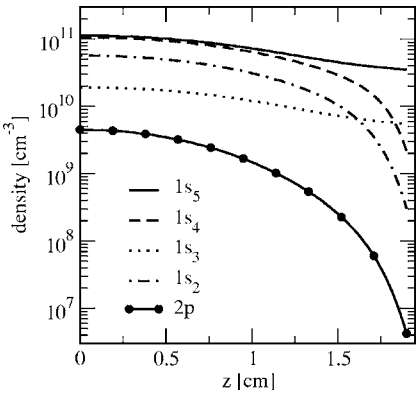

FIG. 2. Axial profiles of steady-state densities of excited argon atoms at p_0=1.33 Pa for geometry A.

sities of excited atoms diminish from their maximum value by more than two orders of magnitude from the discharge center to the electrode. In case of the metastable atoms the diffusion partially compensates the low production rates near the electrode, and thus, their profiles are wider than those of the other excited atoms.

Figure 3 represents the corresponding temporal evolution of the excited atoms in the discharge center during the afterglow. In the absence of the rf electric field the decay of the wall potential causes a depletion of the high-energy part of the EVD. Hence, all ground state excitation rates in electron collisions decrease in time. As a consequence, the populations of the excited states fall off in the afterglow. The short lifetimes of the $2p$ levels cause a rapid decay of the corresponding populations. Because of the large effective lifetimes of the resonance levels Ar($1s_4$) and Ar($1s_2$) their densities diminish more slowly in comparison with those of the $2p$ states. Pronounced changes in the densities of metastable atoms occur during the first 20 μs of the afterglow only. Then, these densities decrease only slightly due to the small loss rates. A detailed analysis of main reaction kinetic processes is given in Sec. III E.

The comparison between calculated and measured line-integrated densities of excited argon atoms at the center of the discharge is shown in Figs. 4 and 5 for varying plasma power and pressure, respectively. Generally, the modeling

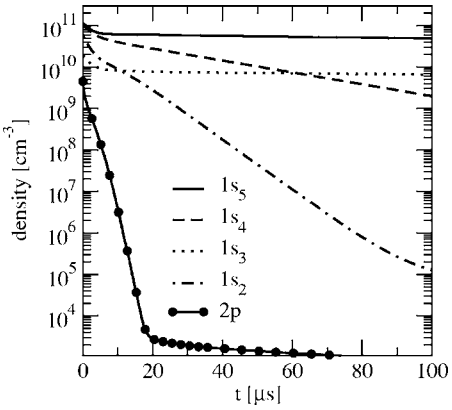

FIG. 3. Temporal evolution of the densities of excited argon atoms in the discharge center at p_0=1.33 Pa for geometry A.

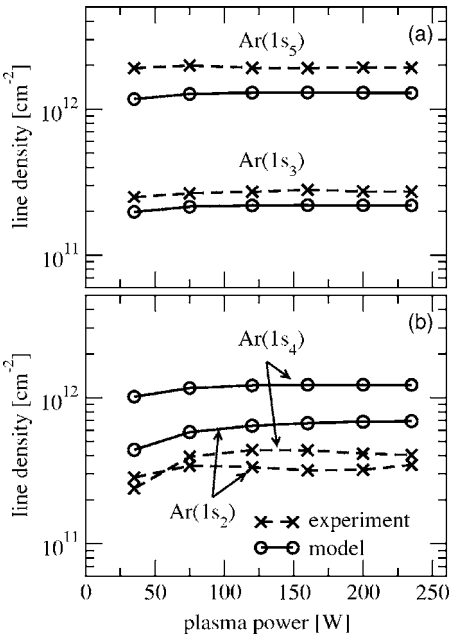

FIG. 4. Line-integrated densities of metastable (a) and resonance (b) atoms for varying plasma power at p_0=1.33 Pa and geometry A.

results show good agreement with the experimental data for the densities of both metastable states. For the resonance atoms the experimental tendencies are well reproduced by the model. However, discrepancies between theoretical and experimental results occur for the absolute values of their densities. The calculated densities of these atoms are higher than measured values by a factor of 3 for Ar($1s_4$) and 2 for Ar($1s_2$). The reason for this behavior is probably the

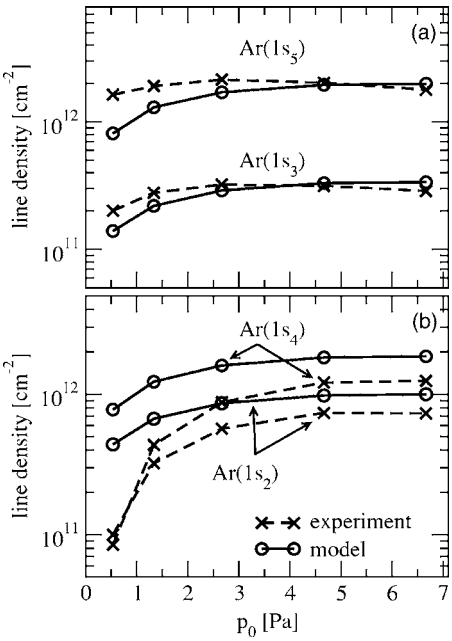

FIG. 5. Line-integrated densities of metastable (a) and resonance (b) atoms as a function of pressure at a plasma power of 160 W and in geometry A.

simplified description of the resonance radiation transport in the model by means of the effective lifetime approximation.

The variation of the plasma power at fixed gas pressure (Fig. 4) has a negligible influence on the densities only. The theoretical analysis clarifies that a larger plasma power causes a larger electron density too. However, the electron density increase is accompanied by a reduction of the mean electron energy. As a consequence, the rate coefficients for both populating and depopulating electron-atom collisions change proportionally to the plasma power, and the excited state densities remain practically independent on the power.

The density variation of the excited argon atoms with increasing gas pressure at constant power (Fig. 5) is similar to that discussed in Fig. 1. The ratio of densities of two metastables $Ar(1s_5)/Ar(1s_3)$ decreases from about 8 at 0.5 Pa to about 6.2 at 7 Pa. These results are in a good agreement with recent measurements of Denda *et al.* [15] where the three-dimensional (3D) profiles of metastable atom densities have been studied at comparable conditions.

In order to get better agreement with experimental results for the resonance atoms a further improvement of the model is required. In particular, a more detailed treatment of the resonance radiation transport is expected to result in an improved coincidence between measured and calculated densities [41].

B. Interaction of excited states and electron kinetics

The results presented in this and the following two subsections refer to the discharge geometry B. The pressure was varied from 2 to 133 Pa at a constant energy density of 30 $\mu J/cm^2$. The corresponding plasma power decreased monotonically from 70 W at the lowest pressure to 7 W at $p_0=133$ Pa.

Figure 6 illustrate the temporal evolution of the isotropic (or energy) distribution $f_0(\varepsilon,t)$ in the center of the discharge during the afterglow at the lowest and highest pressures considered. The depletion of the population of electrons in the range of higher energies progressing in time is mainly caused by the wall losses of electrons. This reduction is strongly pronounced at the pressure of 2 Pa [Fig. 6(a)] and is accompanied by strong structural changes in the energy distribution. Two specific regions in the energy range above 7.5 eV and around 12 eV can be identified for later times where maxima occur caused by the production of electrons in chemoionization processes and superelastic collisions, respectively. The resulting structure is more pronounced at lower pressures due to higher densities of excited atoms [cf. Fig. 1(b)]. Hence, chemoionization processes and superelastic collisions become important in the afterglow plasma also at pressures in the range of a few pascals.

Similar structures in the energy distribution function at higher pressures have been found for other gases as well. The effect of superelestic collisions processes on the formation of local maxima in the energy distribution in the post discharge regime was demonstrated for Ne [9] and H_2 [42,43] as well as for Ar-N_2 [12] and He-Xe [44] mixtures. Local maxima that correspond to chemoionization processes at pressures higher than 0.5 Torr were discussed in Refs. [2,9,10,18,45].

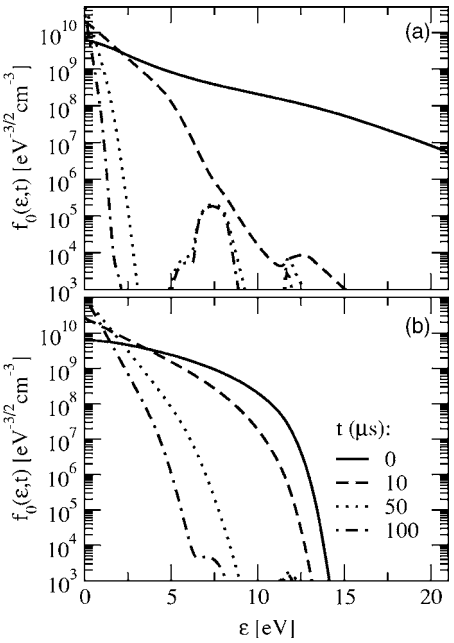

FIG. 6. Temporal evolution of the isotropic distribution $f_0(\varepsilon,t)$ in the discharge center ($z=0$) during the afterglow at $p_0=$(a) 2 and (b) 133 Pa for discharge geometry B.

To check the theoretical results for the electron kinetics, influenced in the afterglow by the complex interplay of diffusive cooling, electron-electron interaction, and the argon kinetics, a comparison with results of probe measurements [3] has been performed. The measured and calculated temporal behavior of the wall potential and the mean electron energy at a pressure of 9 Pa are shown in Fig. 7. Two different reaction kinetics schemes, namely, set A and set B, have been used for the model calculations. Set A takes into ac-

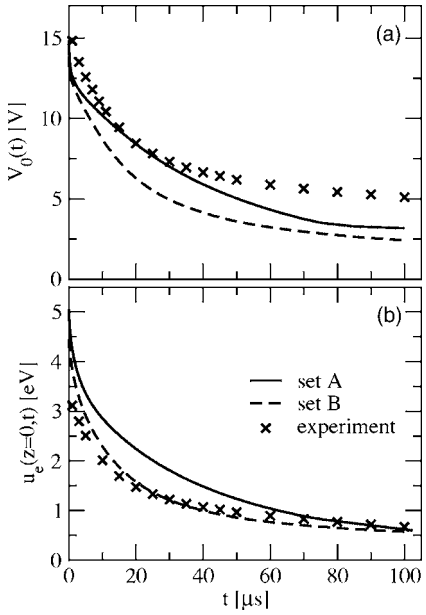

FIG. 7. Decay of (a) the wall potential $V_0(t)$ and (b) mean electron energy in the discharge center $u_e(z=0,t)$ at $p_0=9$ Pa for discharge geometry B.

count only the excitation from the ground state and neglects the impact of the excited states, while set B represents the full kinetic scheme described above. The calculations using set A and B give qualitatively similar results. However, the neglect of the excited states (set A) leads to a slower decrease of the wall potential [Fig. 7(a)] during the first 50 μs in the afterglow. Set B provides much better agreement with the temporal course of the wall potential obtained from the experiments. Remaining discrepancies between experimental and modeling results in the absolute value of the wall potential occur already at steady state and arise probably from simplifications made in the model. It becomes obvious from the comparison between the measured and calculated mean electron energies in the discharge center [Fig. 7(b)], that the excited state kinetics influences remarkably the temporal behavior of the plasma and that its neglect in the model causes an overestimation of the mean energy.

C. Ionization budget of plasma

Applying the factor $(2/m_e)^{1/2}$ to the electron kinetic equation [Eq. (7) in Ref. [22]] followed by the integration over the total energy ε, the global electron particle balance

$$\frac{d\hat{n}_e}{dt} = \langle G_{\mathrm{gr}}^{\mathrm{io}} \rangle + \langle G_{\mathrm{step}}^{\mathrm{io}} \rangle + \langle G_{\mathrm{chem}}^{\mathrm{io}} \rangle - L_{\mathrm{loss}}^{\mathrm{wall}} \tag{5}$$

of the plasma is obtained. Here $\hat{n}_e$ denotes the spatially averaged electron density, $\langle G_{\mathrm{gr}}^{\mathrm{io}} \rangle$, $\langle G_{\mathrm{step}}^{\mathrm{io}} \rangle$, and $\langle G_{\mathrm{chem}}^{\mathrm{io}} \rangle$ are the spatially averaged production rates of the electrons in direct (gr), stepwise (step), and chemo- (chem) ionization and $L_{\mathrm{loss}}^{\mathrm{wall}}$ is the wall loss rate. These quantities have the following representations:

$$\hat{n}_e(t) = \int_0^\infty \hat{B}(\varepsilon,t) f_0(\varepsilon,t) d\varepsilon \tag{6a}$$

$$\langle G_\alpha^{\mathrm{io}} \rangle = \sqrt{\frac{2}{m_{\mathrm{e}}}} \int_0^\infty \left(\frac{1}{z_e} \int_0^{z(\varepsilon)} u \sum_j N_j(z,t) Q_j^\alpha(u) dz \right) f_0(\varepsilon,t) d\varepsilon,$$

$$\alpha = \mathrm{gr}, \mathrm{step}, \tag{6b}$$

$$\langle G_{\mathrm{chem}}^{\mathrm{io}} \rangle = \sqrt{\frac{2}{m_{\mathrm{e}}}} \int_0^\infty \hat{S}_c(\varepsilon,t) d\varepsilon, \tag{6c}$$

$$L_{\mathrm{loss}}^{\mathrm{wall}} = \sqrt{\frac{2}{m_{\mathrm{e}}}} \int_{w(z_e,t)}^\infty L_w(\varepsilon,t) f_0(\varepsilon,t) d\varepsilon, \tag{6d}$$

where $\hat{B}(\varepsilon,t)$ is the axially averaged square root of the kinetic energy, $\hat{S}_c(\varepsilon,t)$ is the averaged inscattering profile times the rate of chemoionization, and $L_w(\varepsilon,t)$ denotes the wall loss factor. These quantities are given by relations (8b), (8h), and (8g) in Ref. [22]. Q_j^{gr} and Q_j^{step} denote the cross sections of electron impact ground state (gr) and stepwise (step) ionization.

Figure 8 displays the spatially averaged electron production and loss rates in dependence on the gas pressure at steady state of the active discharge, i.e., $t=0$ and the instant

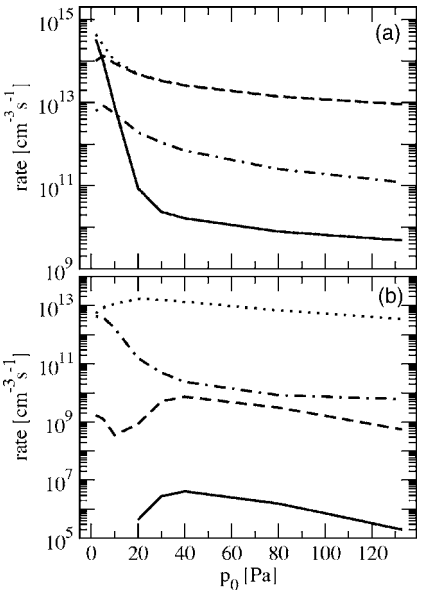

FIG. 8. Pressure dependence of the contributions to the electron gain due to direct ionization (solid line), stepwise ionization (dashed line), and chemoionization (dash-dotted line) and electron wall loss (dotted line) at (a) steady state and (b) $t=100$ μs of the afterglow for geometry B.

$t=100$ μs of the afterglow. At steady state the direct ionization of argon dominates for pressures below 10 Pa, while for higher pressures the contribution of stepwise ionization dominates in the electron production. Chemoionization processes are generally of minor importance at steady state. An increase of the gas pressure at fixed energy density is accompanied by a diminution of the population of excited states [see Fig. 1(b)]. Therefore, all contributions to the particle balance decrease with growing pressure as shown in Fig. 8(a).

During the afterglow represented in Fig. 8(b) almost no contribution of the direct ionization occurs because of the depletion of the population of electrons at higher energies (cf. Fig. 6). Here, the chemoionization processes become predominantly electron particle gain processes and at $p_0=2$ Pa the considerably high population of excited states even causes a compensation of the wall losses by chemoionization processes. At pressures higher than about 30 Pa stepwise ionization gains importance for the electron production as a result of the slower decay of the high-energy part of EVD.

D. Electron power balance

The global power balance of the electrons is obtained by applying the factor $(2/m_e)^{1/2}\varepsilon$ to the kinetic equation of the nonlocal approach [Eq. (7) in Ref. [22]] followed by the integration with respect to the total energy ε. The resulting balance equation gets the representation

$$\frac{d\langle n_e u_e \rangle}{dt} = \langle P^{\mathrm{f}} \rangle + \langle P^{\mathrm{deexc}} \rangle + \langle P^{\mathrm{chem}} \rangle - \langle P^{\mathrm{ela}} \rangle - \langle P^{\mathrm{exc}} \rangle - \langle P^{\mathrm{io}} \rangle - P_{\mathrm{loss}}^{\mathrm{wall}} \tag{7}$$

where $\langle n_e u_e \rangle$ denotes the spatially averaged electron energy

density, $\langle P^{\mathrm{f}}\rangle$, $\langle P^{\mathrm{deexc}}\rangle$, and $\langle P^{\mathrm{chem}}\rangle$ are the spatially averaged power gain rates from the azimuthal electric field and gas heating, deexciting collisions, and chemoionization, respectively. $\langle P^{\mathrm{ela}}\rangle$, $\langle P^{\mathrm{exc}}\rangle$, and $\langle P^{\mathrm{io}}\rangle$ are the spatially averaged power loss rates due to elastic, exciting, and ionizing collisions, and the term $P_{\mathrm{loss}}^{\mathrm{wall}}$ describes the wall loss. These quantities have the representations

$$\langle n_e u_e\rangle = \int_0^\infty \hat{B}(\varepsilon,t) f_0(\varepsilon,t)\varepsilon\, d\varepsilon, \tag{8a}$$

$$\langle P^{\mathrm{f}}\rangle = -\sqrt{\frac{2}{m_{\mathrm{e}}}}\int_0^\infty \hat{D}(\varepsilon,t)\frac{\partial f_0(\varepsilon,t)}{\partial\varepsilon}d\varepsilon, \tag{8b}$$

$$\langle P^{\mathrm{ela}}\rangle = \sqrt{\frac{2}{m_{\mathrm{e}}}}\int_0^\infty \hat{G}(\varepsilon,t) f_0(\varepsilon,t)d\varepsilon, \tag{8c}$$

$$\langle P^{\alpha}\rangle = \sqrt{\frac{2}{m_{\mathrm{e}}}}\int_0^\infty \sum_i U_i^\alpha \hat{H}_i^\alpha f_0(\varepsilon,t)d\varepsilon, \quad \alpha = \mathrm{deexc,exc,io}, \tag{8d}$$

$$\langle P^{\mathrm{chem}}\rangle = \sqrt{\frac{2}{m_{\mathrm{e}}}}\int_0^\infty \hat{S}_c(\varepsilon,t)\varepsilon\, d\varepsilon, \tag{8e}$$

$$P_{\mathrm{loss}}^{\mathrm{wall}} = \sqrt{\frac{2}{m_{\mathrm{e}}}}\int_{w(z_e,t)}^\infty L_w(\varepsilon,t) f_0(\varepsilon,t)\varepsilon\, d\varepsilon. \tag{8f}$$

$\hat{G}(\varepsilon,t)$ includes the elastic energy transfer and $\hat{D}(\varepsilon,t)$ includes the rf electric field. These quantities are given by formulas (8d) and (8e) in Ref. [22]. The term $\hat{H}_i^\alpha$ with α =deexc, exc, io describes the individual gain in deexciting (deexc) and loss in exciting (exc) or ionizing (io) collisions, respectively, and is determined according to Eq. (8f) in Ref. [22] taking into account each electrom-atom collision process separately. U_i^α denotes the respective energy gain or loss in the corresponding collision process.

Figure 9 shows the contributions to the electron power balance in dependence on the gas pressure at steady state of the active discharge and $t=100$ μs of the afterglow. The dominating power gain process at steady state is the gain from the electric field, while the contribution of deexcitation and chemoionization processes is negligible. In the pressure range from 2 to about 70 Pa the exciting collisions represent the main loss mechanism for the electrons. At higher pressures elastic collisions gain a comparable impact as the excitation processes on the power balance. Wall losses gain some importance only at very low pressures with a contribution of about 10% to the total power loss rate. All other processes are insignificant at steady state.

This picture changes completely during the afterglow as illustrated by Fig. 9(b). In the absence of the electric field the main power gain results from chemoionization processes at pressures below 10 Pa. Around 20 Pa the gain rates of chemoionization processes, deexciting collisions, and heating by the gas have almost the same value. At further increase of the pressure the gas heating becomes the leading power gain contribution. Concerning the contributions to the total power loss, wall losses are dominant at pressures below 40 Pa, while for higher pressures the power is dissipated mainly in elastic collisions again. The excitation processes contribute to less than 15% to the total power loss and ionization processes are unimportant.

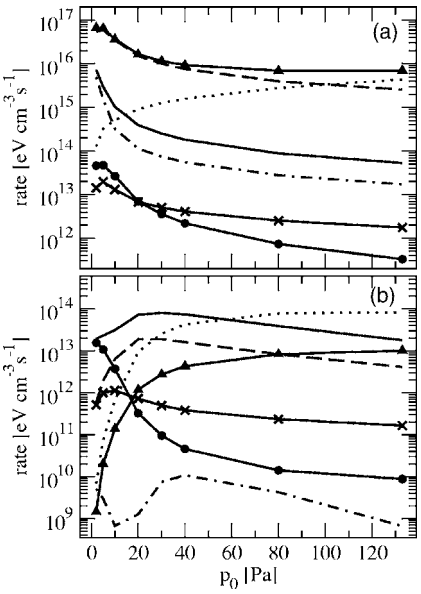

FIG. 9. Pressure dependence of the contributions to the electron power gain due to field and gas heating (triangles), deexciting collisions (crosses), and chemoionization (circles) and power losses due to wall losses (solid line), elastic (dotted line), exciting (dashed line), and ionizing (dash-dotted line) collisions at (a) steady state and (b) $t=100$ μs of the afterglow for geometry B.

E. Main reaction kinetics pathways

Emphasis has been put in the model on a detailed description of the kinetics of excited argon atoms. In Fig. 10 the most important processes in the steady-state balance of the excited atoms at the gas pressure of 2 Pa are illustrated,

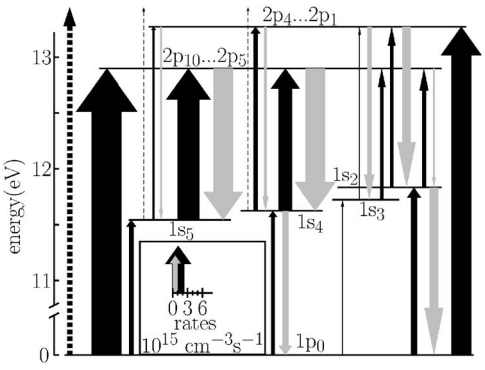

FIG. 10. Most important production and destruction rates of excited atoms for $p_0=2$ Pa and geometry B at steady state. Excitation and deexcitation in electron collisions (solid black arrows), radiation (solid gray arrows), and ionization (dashed arrows). The width of the arrows illustrates the magnitude of the rates.

where rates smaller than 10^{15} cm^{-3} s^{-1} were omitted in the scheme. The discussion refers to the discharge center of the geometry B at an energy density of 30 μJ/cm^2 and a plasma power of 70 W. The corresponding densities of excited atoms are shown in Fig. 1(b).

The balance of the Ar($1s_5$) and Ar($1s_4$) level, respectively, is dominated by the strong coupling with the group of Ar($2p_{10}$),…, Ar($2p_5$) levels via $1s_5$ and $1s_4$ excitation to this $2p$ group in electron collisions and infrared radiation back to both states. In this way, there is also a transition from the Ar($1s_5$) to the Ar($1s_4$) level which is more effective than direct electron impact excitation and quenching. However, the transition rates between the Ar($1s_5$) level and the group of Ar($2p_{10}$),…, Ar($2p_5$) levels balance each other to a large extent. Consequently, the net change is small in comparison with the rates of other processes which influence the population of the corresponding levels. In the case of the Ar($1s_5$) level these processes are the production by ground state excitation and loss due to electron impact excitation to the Ar($2p_4$),…, Ar($2p_1$) levels. A similar situation occurs for the Ar($1s_4$) level whose population is additionally influenced by the loss due to resonance radiation.

The density of the metastable Ar($1s_3$) level is mainly determined by the ground state excitation, stepwise excitation to the $2p$ levels, and infrared radiation from the Ar($2p_4$) and Ar($2p_2$) level. Notice that the production and destruction rates for the Ar($1s_3$) level are small compared to those of the other levels. The balance of the Ar($1s_2$) level is controlled by the gain due to ground state excitation and radiative transitions of the $2p_4$-$2p_1$ levels as well as loss in resonance radiation and excitation to the $2p$ states. Quenching processes of excited states by argon atoms are generally negligible because the pressure is low.

The ground state ionization in electron collisions is by far the most important electron production channel. The ionization rates of the levels $1s_5$ and $1s_4$ are together about 10% of that of the ground state. All other ionization rates are not displayed in Fig. 10 because they are lower than 5×10^{13} cm^{-3} s^{-1}.

The corresponding most important rates of population and depopulation of excited argon levels at the instant $t=100$ μs of the afterglow are shown in Fig. 11. Here, rates smaller than 10^{11} cm^{-3} s^{-1} were neglected in the scheme. Notice that the ionization rates presented in this figure are due to the chemoionization processes of corresponding levels.

In consequence of the strong depletion of the high energy part of the EVD at this instant [see Fig. 6(a)] almost no excitation and ionization from the ground state occurs. In contrast to this finding the high population of the energy region below 3 eV in the EVD results in a growing importance of the electron impact excitation and deexcitation processes with small thresholds, like the transfer between neighboring levels. The most important depopulation processes of the Ar($1s_5$) level are the excitation to other $1s$ levels and chemoionization processes. Latter contribute with about 90% to the total ionization rate during the afterglow. Deexciting electron collisions with Ar($1s_4$) and Ar($1s_3$) atoms represent the most important contributions among the particle gain

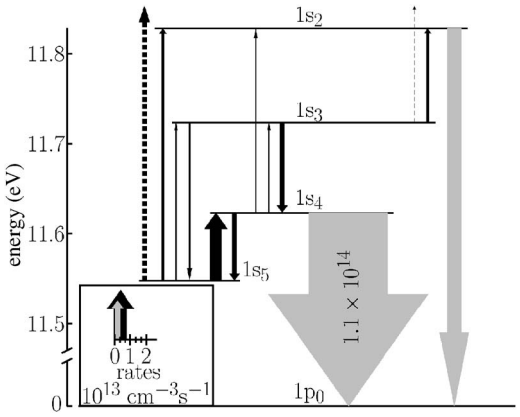

FIG. 11. The same as in Fig. 10, but at $t=100$ μs of the afterglow.

processes for the Ar($1s_5$) level. The total particle loss rate is not compensated by the total gain rate and consequently the Ar($1s_5$) density slowly decreases (cf. Fig. 3). The balance of the Ar($1s_4$) level is dominated by the resonance radiation loss whose rate is by more than two orders of magnitude larger than that of all other processes. The excitation to Ar($1s_2$) and deexcitation to the Ar($1s_5$) and Ar($1s_4$) states in electron collisions determine the decay rate of the Ar($1s_3$) level. Electron impact excitation of the lower-lying $1s$ levels and the resonance radiation are the substantial processes for the balance of the Ar($1s_2$) atoms.

IV. SUMMARY

The influence of the excited atoms and their collision and radiation processes on the characteristics of decaying plasmas in argon at pressures between 0.5 and 133 Pa has been studied by means of a self-consistent model which uses the nonlocal approach for the kinetic treatment of the electrons. Special attention has been paid to the determination of the densities of excited argon atoms as well as to the analysis of their impact on the electron energy distribution, ionization kinetics and electron power balance.

The model predicts quite high densities of excited atoms for pressures of a few pascals and a decrease of the densities with increasing pressure at fixed electron energy density. The significant population of the excited levels leads to large structural changes of the electron energy distribution in the afterglow phase. In particular, two maxima occur in the distribution function at energies around 7.5 eV mainly resulting from chemoionization processes and around 12 eV basically caused by superelastic electron collisions.

The analysis of the ionization kinetics of the electrons clarifies that the stepwise ionization processes are predominant at steady state, while chemoionization processes become leading for the electron production during the afterglow.

At steady state the excited argon atoms influence the power budget mainly due to the power loss in stepwise excitation which dominates for pressures below about 50 Pa and is comparable to the power loss in elastic electron colli-

sions at higher pressures. During the afterglow chemoionization processes and deexciting electron collisions primarily provide power gain of the electron ensemble at pressures below about 10 Pa and the contribution of the excited atoms to the total power loss generally remains smaller than about 15%.

The comparison of calculations by means of the generalized model with experimental data for metastable argon atoms for the wall potential and mean electron energy generally showed good agreement and additionally clarified the distinct impact of the excited atoms on the behavior of low-pressure discharges plasmas. The remaining discrepancies between measured and calculated densities of the resonance atoms suggest an improvement of the reaction kinetic model of the excited atoms, in particular with respect to a more accurate treatment of resonance radiation transport. This is planned for future studies.

ACKNOWLEDGMENTS

The work was supported by the Deutsche Forschungsgemeinschaft Project No. Uh 106/2-1.

[1] N. Kolokolov, A. Kudryavtsev, and O. Toronov, Sov. Phys. Tech. Phys. **30**, 1128 (1985).
[2] V. Demidov, N. Kolkolov, and O. Toronov, Sov. J. Plasma Phys. **12**, 402 (1988).
[3] A. Maresca, K. Orlov, and U. Kortshagen, Phys. Rev. E **65**, 056405 (2002).
[4] L. Sirghi, K. Ohe, and T. Kimura, Phys. Plasmas **4**, 1160 (1997).
[5] R. R. Arslanbekov and A. A. Kudryavtsev, Phys. Rev. E **58**, 7785 (1998).
[6] R. Arslanbekov, A. Kudryavtsev, and L. Tsendin, Phys. Rev. E **64**, 016401 (2001).
[7] F. Tochikubo, Z. Lj. Petrović, S. Kakuta, N. Nakano, and T. Makabe, Jpn. J. Appl. Phys., Part 1 **33**, 4271 (1994).
[8] G. Wenig, M. Schulze, P. Awakowicz, and A. v. Keudell, Plasma Sources Sci. Technol. **15**, S35 (2006).
[9] T. Bräuer, S. Gortchakov, D. Loffhagen, S. Pfau, and R. Winkler, J. Phys. D **30**, 3223 (1997).
[10] N. A. Gorbunov, N. B. Kolokolov, and F. E. Latyshev, Tech. Phys. **46**, 391 (2001).
[11] V. I. Kolobov, G. J. Parker, and W. N. G. Hitchon, Phys. Rev. E **53**, 1110 (1996).
[12] N. A. Dyatko, Y. Z. Ionikh, N. B. Kolokolov, A. V. Meshanov, and A. P. Napartovich, J. Phys. D **33**, 2010 (2000).
[13] M. Tadokoro, H. Hirata, N. Nakano, Z. Lj. Petrović, and T. Makabe, Phys. Rev. E **58**, 7823 (1998).
[14] H. Hirata, M. Tadokoro, N. Nakano, Z. Lj. Petrović, and T. Makabe, IEEE Trans. Plasma Sci. **27**, 50 (1999).
[15] T. Denda, Y. Miyoshi, Y. Komukai, T. Goto, Z. Lj. Petrović, and T. Makabe, J. Appl. Phys. **95**, 870 (2004).
[16] G. A. Hebner, J. Appl. Phys. **80**, 2624 (1996).
[17] K. Hioki, N. Itazu, Z. Lj. Petrović, and T. Makabe, Jpn. J. Appl. Phys., Part 2 **40**, L1183 (2001).
[18] L. J. Overzet and J. Kleber, Plasma Sources Sci. Technol. **7**, 512 (1998).
[19] D. P. Lymberopoulos and D. J. Economou, J. Appl. Phys. **73**, 3668 (1994).
[20] M. W. Kiehlbauch and D. B. Graves, J. Appl. Phys. **91**, 3539 (2002).
[21] T. Sato and T. Makabe, J. Appl. Phys. **98**, 113304 (2005).
[22] S. Gorchakov, D. Uhrlandt, M. J. Hebert, and U. Kortshagen, Phys. Rev. E **73**, 056402 (2006).
[23] L. D. Tsendin, Sov. Phys. JETP **39**, 805 (1974).
[24] J. E. Velazco, J. H. Kolts, and D. W. Setser, J. Chem. Phys. **69**, 4357 (1978).
[25] H. Lange, F. Leipold, M. Otte, S. Pfau, and D. Uhrlandt, Plasma Chem. Plasma Process. **19**, 255 (1999).
[26] V. Zeman, K. Bartschat, C. Norén, and J. W. McConkey, Phys. Rev. A **58**, 1275 (1998).
[27] K. Bartschat and V. Zeman, Phys. Rev. A **59**, R2552 (1999).
[28] O. Zatsarinny and K. Bartschat, J. Phys. B **37**, 4693 (2004).
[29] M. Schaper and H. Scheibner, Contrib. Plasma Phys. **9**, 43 (1969).
[30] J. B. Boffard, G. A. Piech, M. F. Gehrke, L. W. Anderson, and C. C. Lin, Phys. Rev. A **59**, 2749 (1999).
[31] D. Rapp and P. Englander-Golden, J. Chem. Phys. **43**, 1464 (1965).
[32] H. Deutsch, K. Becker, S. Matt, and T. Märk, J. Phys. B **32**, 4249 (1999).
[33] A. J. Dixon, M. F. A. Harrison, and A. C. H. Smith, Contributed Papers of the 8th International Conference on the Physics of Electronic and Atomic Collisions (ICPEAC), Belgrade, 1973, p. 405.
[34] C. Yamabe, S. J. Buckman, and A. V. Phelps, Phys. Rev. A **27**, 1345 (1983).
[35] W. L. Wiese, J. W. Braulth, K. Danzmann, V. Helbig, and M. Kock, Phys. Rev. A **39**, 2461 (1989).
[36] A. Irimia and F. C. Fischer, J. Phys. B **37**, 1659 (2004).
[37] N. B. Kolokolov, A. A. Kudrjavtsev, and A. B. Blagoev, Phys. Scr. **50**, 371 (1994).
[38] N. Sadeghi and D. W. Setser, J. Chem. Phys. **115**, 3144 (2001).
[39] T. D. Nguyen and N. Sadeghi, Phys. Rev. A **18**, 1388 (1978).
[40] R. F. S. Chang and D. W. Setser, J. Chem. Phys. **69**, 3885 (1978).
[41] Yu. B. Golubovskii, I. A. Porokhova, H. Lange, S. Gortchakov, and D. Uhrlandt, Plasma Sources Sci. Technol. **14**, 45 (2005).
[42] K. Hassouni, A. Gicquel, and M. Capitelli, Phys. Rev. E **59**, 3741 (1999).
[43] G. Lombardi, X. Duten, K. Hassouni, M. Capitelli, and A. Gicquel, Eur. Phys. J. D **30**, 225 (2004).
[44] R. Bussiahn, S. Gortchakov, H. Lange, and D. Loffhagen, J. Phys. D **39**, 66 (2006).
[45] V. A. Sheverev, V. P. Stepaniuk, and G. G. Lister, J. Appl. Phys. **92**, 3454 (2002).